

Multi-channel programmable power supply with temperature compensation for silicon sensors

R. A. Shukla, V. G. Achanta, S. R. Dugad^{*}, J. Freeman, C. S. Garde, S. K. Gupta, P. D. Khandekar, A. M. Kurup, S. S. Lokhandwala^{*}, S. Los, S. S. Prabhu, and P. S. Rakshe

Citation: *Review of Scientific Instruments* **87**, 015114 (2016); doi: 10.1063/1.4940424

View online: <http://dx.doi.org/10.1063/1.4940424>

View Table of Contents: <http://aip.scitation.org/toc/rsi/87/1>

Published by the *American Institute of Physics*

Applied Physics
Reviews

SAVE THE DATE!
3D Bioprinting: Physical and Chemical Processes
May 2–3, 2017 • Winston Salem, NC, USA

The background of the banner features a blue-toned image of a human hand with glowing blue veins, set against a dark blue background with a subtle grid pattern.

Multi-channel programmable power supply with temperature compensation for silicon sensors

R. A. Shukla,¹ V. G. Achanta,¹ S. R. Dugad,^{1,a)} J. Freeman,² C. S. Garde,³ S. K. Gupta,^{1,4}
P. D. Khandekar,³ A. M. Kurup,¹ S. S. Lokhandwala,^{1,b)} S. Los,² S. S. Prabhu,¹
and P. S. Rakshe^{3,4}

¹Tata Institute of Fundamental Research, Mumbai 400005, India

²Fermi National Accelerator Laboratory, Batavia, Illinois 60510, USA

³Vishwakarma Institute of Information Technology, Pune 411048, India

⁴GRAPES-3 Experiment, Cosmic Ray Laboratory, Raj Bhavan, Ooty 643001, India

(Received 9 November 2015; accepted 10 January 2016; published online 27 January 2016)

Silicon Photo-Multipliers (SiPMs) are increasingly becoming popular for discrete photon counting applications due to the wealth of advantages they offer over conventional photo-detectors such as photo-multiplier tubes and hybrid photo-diodes. SiPMs are used in variety of applications ranging from high energy physics and nuclear physics experiments to medical diagnostics. The gain of a SiPM is directly proportional to the difference between applied and breakdown voltage of the device. However, the breakdown voltage depends critically on the ambient temperature and has a large temperature co-efficient in the range of 40-60 mV/°C resulting in a typical gain variation of 3%-5%/°C [Dinu *et al.*, in *IEEE Nuclear Science Symposium, Medical Imaging Conference and 17th Room Temperature Semiconductor Detector Workshop* (IEEE, 2010), p. 215]. We plan to use the SiPM as a replacement for PMT in the cosmic ray experiment (GRAPES-3) at Ooty [Gupta *et al.*, *Nucl. Instrum. Methods Phys. Res., Sect. A* **540**, 311 (2005)]. There the SiPMs will be operated in an outdoor environment subjected to temperature variation of about 15 °C over a day. A gain variation of more than 50% was observed for such large variations in the temperature. To stabilize the gain of the SiPM under such operating conditions, a low-cost, multi-channel programmable power supply (0-90 V) was designed that simultaneously provides the bias voltage to 16 SiPMs. The programmable power supply (PPS) was designed to automatically adjust the operating voltage for each channel with a built-in closed loop temperature feedback mechanism. The PPS provides bias voltage with a precision of 6 mV and measures the load current with a precision of 1 nA. Using this PPS, a gain stability of 0.5% for SiPM (Hamamatsu, S10931-050P) has been demonstrated over a wide temperature range of 15 °C. The design methodology of the PPS system, its validation, and the results of the tests carried out on the SiPM is presented in this article. The proposed design also has the capability of gain stabilization of devices with non-linear thermal response. © 2016 AIP Publishing LLC. [<http://dx.doi.org/10.1063/1.4940424>]

I. INTRODUCTION

Silicon Photo-Multipliers (SiPMs) are regarded as superior photo-detectors over conventionally used Photo-Multiplier Tubes (PMTs). The key advantages of SiPM include a high gain ($\sim 10^6$), immunity to magnetic field, a compact footprint, higher photon detection efficiency (PDE), low bias voltage (30-100 V) and a small power budget.³ Thus, SiPMs have become a viable replacement for traditional PMTs,⁴ and are being used in several applications ranging from medical imaging (PET cameras)⁵⁻⁷ to high-energy, and nuclear physics experiments like CMS and T2K.⁸⁻¹² The cosmic ray experiment, GRAPES-3, being conducted at Ooty, consists of an array of scintillators and a large area muon detector,¹³ sampling electromagnetic and muon components of air showers induced by cosmic rays² in the range 3×10^{13} – 10^{16} eV. Conventional PMTs are used to convert the scintillation light

to an electrical signal. We propose to replace the PMTs with SiPMs due to several advantages offered by this new generation of solid-state photo-device. The scintillator detectors used in the GRAPES-3 experiment operate in an ambient environment with a day-night temperature variation of about 15 °C. Therefore, it is essential to design a customized low-cost power supply that can stabilize the gain of a SiPM over a wide range of temperatures.

SiPM with a typical size of a few mm² consists of an array of densely packed Avalanche Photo-Diodes (APDs). The size of an APD cell in the SiPM is about 50 $\mu\text{m} \times 50 \mu\text{m}$. An array of large number of APDs have a common anode rail and connect to a common cathode rail through a series resistor for each APD, referred as the quenching resistor. The SiPM is reverse biased above the breakdown voltage (V_{bd}) to attain a gain comparable to that of a PMT. The gain of SiPM depends on the difference between applied bias and breakdown voltage of the device ($\Delta V = V_{bias} - V_{bd}$), referred to as *over voltage*. Individual APDs of the SiPM designed to have identical gain, generate a fixed amount of charge on detection of a photon(s), resulting in a digital signal. The sum of all the individual APD

^{a)}Electronic mail: dugad@cern.ch

^{b)}Present address: University of Edinburgh, Edinburgh EH8 9YL, United Kingdom.

signals results in an analog signal, indicating the number of APDs triggered by incident photons or thermal generation of *electron-hole* pairs.

The SiPM has already generated a lot of interest within the experimental community. Macroscopic and microscopic characteristics of this device have been studied by several groups.^{3,14} These studies have highlighted effects of limitations of this device such as dark counts, dependence of breakdown voltage on the temperature,¹ cross talk, etc. in various applications. The dependence of the breakdown voltage on temperature is of particular interest, as the gain of the device critically depends on the *over voltage*. The temperature coefficient of V_{bd} is typically 40-60 mV/°C^{1,15} resulting in a gain variation of about 3%-5%/°C. This can severely limit the application of this device in the outdoor environment such as the GRAPES-3 experiment. The gain of the device has to be kept stable within 1% for a successful operation in this experiment. In addition, there are other temperature dependent factors, such as cross talk, after pulsing, photon detection efficiency, and dark count rate that needs to be considered while evaluating appropriate choice of SiPM for such experiments.

The gain of a SiPM can be stabilized by maintaining the device at a stable temperature using thermo-electric coolers. While this approach is effectively used in the outer hadron calorimeter of the CMS detector,¹⁰ it has certain limitations. The thermo-electric coolers are effective over a relatively small temperature range, thus, are difficult to use in outdoor conditions. Second, the thermal as well as power budget can become unacceptably large with this approach. An alternative approach is to maintain stable gain by operating the device with a constant *over voltage* at all temperatures. This implies that the bias voltage needs to be adjusted dynamically as a function of the temperature. This method can compensate for a larger thermal swing present in GRAPES-3 like environment. It can be implemented in variety of ways such as, closed loop feedback of the device dark current or use of thermistors to compensate for drift in the *over voltage*.^{11,16-18} However, many of these methods do not deliver adequate stability over a large temperature range.

In this article, we present the design and performance of a multi-channel (16 channels) programmable power supply (PPS) system optimized to the requirements of the GRAPES-3 experiment. It provides the required stability of gain (0.5%) demonstrated over a wide temperature range (15 °C) and is a cost effective solution. The PPS system is essentially a closed loop feedback system implemented using high resolution programmable linear regulators and high precision temperature feedback with an easy to use interface. The Secs. II and III present construction and working principle of the design followed by the calibration and validation of the design. In Section IV, the operation of SiPM, powered by the PPS developed in-house, has been demonstrated for gain stability over a wide range of temperatures.

II. DESIGN OF SiPM PPS SYSTEM

As discussed earlier, the gain of a SiPM is directly proportional to the *over voltage*, thus, a small change in the *over voltage* can cause a significant change in the gain of SiPM.

The temperature coefficient of the breakdown voltage of a SiPM causes a gain change of about 3%-5%/°C. Therefore, the applied voltage needs to be dynamically adjusted every 0.1 °C change to attain the desired gain stability. Hence, voltage resolution of the system must be ~6 mV. The current flowing through the SiPM during test was about 150 nA at room temperature (22 °C) and nominal operating voltage as specified by the manufacturer. A current resolution of ~0.1% is adequate to accurately measure the current flowing through the SiPM. The required design specification of PPS is summarized in Table I. The design and working principles of PPS fabricated for large-scale operation of SiPMs in the ongoing GRAPES-3 experiment are discussed in present section. The PPS system is quite compact ($9 \times 10 \text{ cm}^2$) and was designed to supply bias voltage with adequate capacity to drive 16 SiPMs, independently along with a provision to measure the current flowing through each channel. In Fig. 1 the block diagram of the multi-channel PPS is shown. It consists of (a) Cockcroft-Walton high voltage generator module, (b) Digital to Analog Converter (DAC) facilitating programmable feature of bias voltage generation, (c) Array of discrete linear regulators used as voltage drop elements for each channel, (d) Solid state temperature sensors, (e) Analog to Digital Converters (ADCs) used for measuring current flowing through each channel and temperature at different locations, and (f) 8-bit PIC micro-controller that controls the operation of the PPS system and communicates with the PC using USB protocol. Algorithms for dynamically evaluating the bias voltage based on the thermal response of the breakdown voltage were also encoded in the micro-controller.

A. High voltage generator module

A Cockcroft-Walton multiplier consisting of 10 stages was used to generate the required high voltage (110 V) on-board, from a DC input of 6.5 V. The AC drive needed for the multiplier was generated using an operational amplifier based RC oscillator operating at 16 KHz. The voltage multiplier circuit was developed as a separate pluggable module making the system modular and easy to maintain. The high voltage was then distributed to 16 independent programmable linear regulators to provide the desired bias voltage for each SiPM.

B. Programmable linear regulator

A simplified electrical schematic of programmable high voltage linear regulator and the current monitoring scheme employed in the PPS system are shown in Fig. 2. Each channel

TABLE I. Design specifications of the PPS system for SiPMs.

Specifications	Value
Bias channels per board	16
Voltage range	0-90 V
Voltage resolution	6 mV
Current measurement range	0-32 μ A
Current measurement resolution	0.1% \pm 1 nA
Temperature measurement resolution	0.1 °C

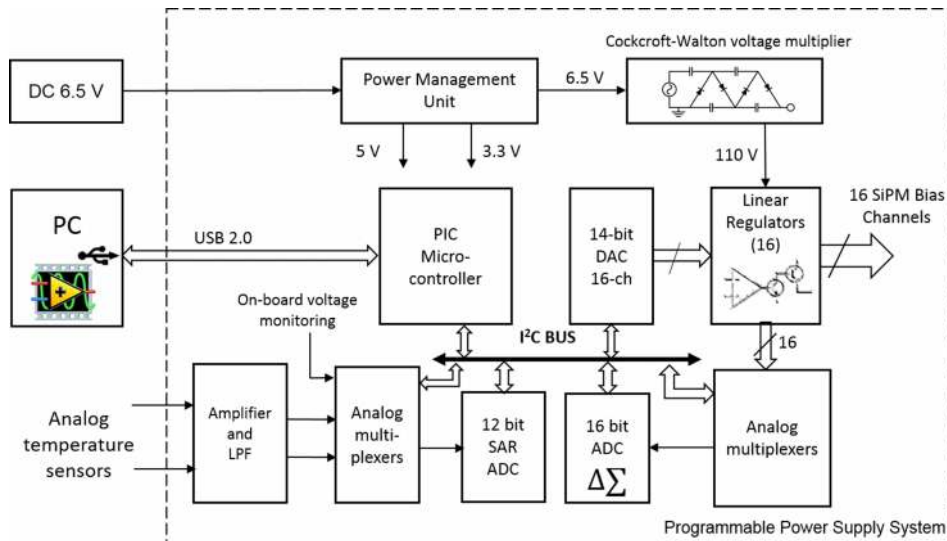


FIG. 1. Block diagram of multi-channel programmable power supply (PPS) system.

consists of a programmable linear regulator constructed with an error amplifier and a series pass transistor. The series pass transistor functions as a programmable resistor, thus, generating the desired voltage drop between the high voltage input (110 V) and the load. The error amplifier drives the series pass transistor proportional to the error (reference–feedback voltage), changing the voltage across the transistor. This change in the transistor voltage drop changes the output voltage across the load, which is then fed back to the amplifier through a feedback network. This action continues until the error gets nullified, thus, maintaining the desired output voltage. This mechanism results in the output voltage being continuously regulated at a constant value proportional to the reference voltage set by the DAC. A high precision 14-bit DAC with a voltage resolution of 0.153 mV was used to generate the reference voltage for an array of discrete linear regulators resulting in the desired precision of 6.25 mV in the applied voltage with a dynamic range of 0-90 V. The calibration procedure, load regulation, and stability of system are presented in Section III.

C. Current and temperature measurement

The measurement of current flowing through the SiPM was achieved by measuring the voltage developed across a small sense resistor (4.99 k Ω), put in series with the load path as shown in Fig. 2. This voltage was amplified by an operational amplifier of gain 12.5 and then fed to the 16-bit delta-sigma ADC through analog multiplexers. The dynamic range of the current measurement was 32 μ A with a precision of 0.1% \pm 1 nA. The procedure for calibrating each channel by measuring current is discussed in Section III. It is to be noted that, the small voltage drop across the sense resistor was also taken into account while calibrating each channel as described in Section III.

Accurate measurement of the temperature was a key requirement for reliable operation of the thermal compensation scheme. A solid state sensor TSIC 501F mounted in the vicinity of SiPM was used to measure the temperature with an accuracy of 0.1 $^{\circ}$ C. The analog output of the sensor, with proper signal conditioning, was first amplified with a gain of 2.5 to utilize the entire dynamic range of the ADC for a temperature range between -10° C and 60 $^{\circ}$ C. A 12-bit successive approximation ADC was used to convert the sensor output voltage into a digital format. 64 successive samples were accumulated and averaged to achieve a good accuracy in temperature measurement.

D. System integration and operation

The PPS system was centrally controlled by an 8-bit micro-controller (Microchip PIC 18F). This controller was responsible for setting up appropriate DAC counts to get desired bias voltage for each channel, measuring ambient temperature, and current through each channel, and for dynamically adjusting the bias voltage to compensate for change in temperature. In addition, the micro-controller monitored abnormal operating conditions to shut down the channels operating beyond the specified tolerance limits. The micro-controller communicated to the user PC via full speed USB

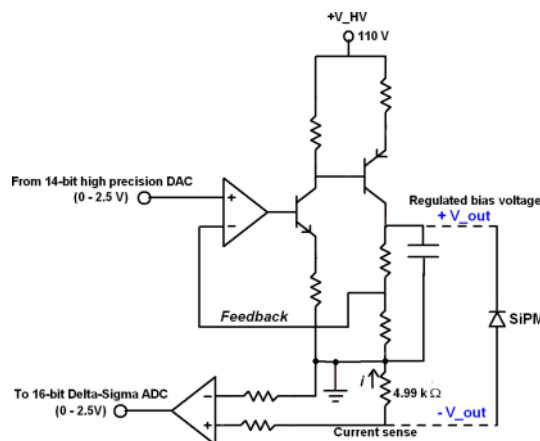


FIG. 2. Schematic of the programmable linear regulator with current sensing mechanism for one channel.

2.0 bus to obtain control parameters from the user. The system also logged the status information, and the measurements of current and temperature to the PC continuously. The complete algorithm for configuring various components of the system, measurement of temperature, and closed loop bias voltage control have been embedded into the micro-controller firmware. Thus, the system can be operated in a standalone mode. An optional I²C port was also provided to communicate with the PPS board (not used in the present work), thus making provision for connecting multiple (up to 128) boards on a common I²C bus. This provided a capability of powering a large number of SiPMs as required for the array of scintillation detectors in the GRAPES-3 experiment.

III. CALIBRATION AND VALIDATION OF PPS

Various components such as the resistors, capacitors, operational amplifiers, transistors and even the DAC may exhibit minor non-linearity over the full operating range of parameters. These discrete components also have a finite tolerance of specified performance parameters. Therefore, it was important to carefully calibrate and then validate the performance of each channel of the PPS. A channel was first calibrated and then tested thoroughly for its accuracy, resolution, driving capacity, and stability prior to actual operation of SiPM. The PPS system has performed very well, exceeding the specifications listed in Table I. The data acquisition system was developed on Linux platform and consisted of (a) LabVIEW¹⁹ based module to control and operate the commercial instruments such as the high precision Keithley pico-ammeter, voltmeter, waveform generator, and the VME system used for data acquisition and (b) standalone PPS-DAQ module that communicated with the PIC micro-controller in the PPS system for acquiring the data or for sending control parameters to the board. Both of these modules, though executing independently, were linked together to synchronize the operation of the modules in the system.

A. System calibration

As mentioned in Sec. II, a programmable bias voltage for the load was generated using a high voltage source and a DAC controlled linear regulator. A digital number corresponding to desired voltage was sent to the PPS board to generate the output voltage. However, due to tolerance of various components in the chain, it became important to establish the relationship between the DAC count and the actual voltage that appeared at the load. Each channel in the system was calibrated using a rigorous procedure. The block diagram of the calibration setup is shown in Fig. 3. The K2000 voltmeter has an input impedance of 10 G Ω in 0-10 V range and 10 M Ω above 10 V. An externally connected load of 10 M Ω appears in parallel with the inputs impedance of the voltmeter. Thus, effective load seen by the PPS system becomes 10 M Ω below 10 V and 5 M Ω above 10 V. Using this setup, calibration and validation runs were taken for each channel.

In the calibration run, counts in steps of 82 (~0.5 V) were sent to the DAC by the micro-controller for a channel under

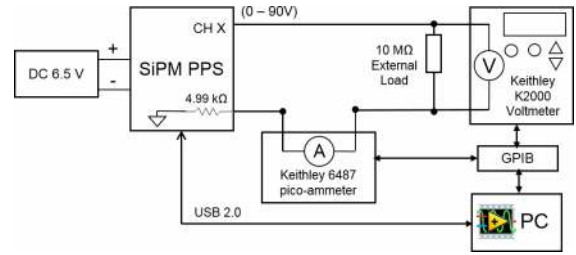


FIG. 3. Block diagram of experimental setup for calibration of the PPS system.

calibration. The voltage generated by the DAC counts across the effective load was measured with a resolution of 0.1 mV using a commercial Keithley voltmeter (Model: K2000). The current flowing in the load was recorded using Keithley pico-ammeter (Model: K6487). In addition, the ADC counts corresponding to the voltage across sense resistor generated by the current in the same load was also recorded. The voltage and current measured by high precision Keithley instruments are referred as *true voltage* and *true current*. These data were used to establish the relationship between the voltage set and DAC counts as well as between the load current and ADC counts. The output voltage (V_{out}) was obtained by

$$V_{out} = \text{true_voltage} + 4990 \times \text{true_current}. \quad (1)$$

In Fig. 4(a), the linear dependence of the measured output voltage (V_{out}) obtained using Equation (1) on the DAC counts is clearly seen. The operating range of 0-90 V was sub-divided into nine segments of 10 V each. A linear fit was performed in each of these segments, and the fit parameters were stored in the database. The dependence of the *true* load current on the ADC counts is shown in Fig. 4(b). The gap in the data around

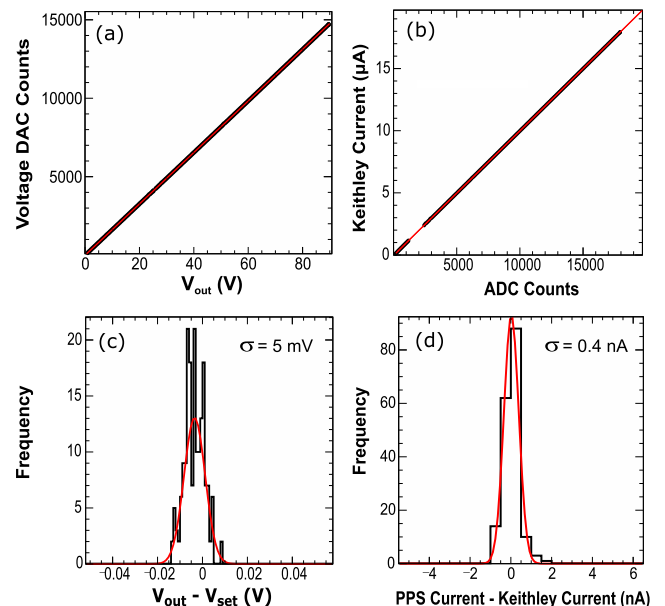


FIG. 4. Dependence of (a) measured output voltage on DAC count and (b) ADC counts on *true* load current. Linear fits in sub-divided ranges are used to obtain calibration parameters. (c) Distribution of difference between set voltage (V_{set}) and measured output voltage (V_{out}) voltage obtained in the range of 0-90 V. (d) Distribution of difference between load current measured with PPS system and *true* current measured by Keithley pico-ammeter.

$2 \mu\text{A}$ was observed due to abrupt change in the effective load from $10 \text{ M}\Omega$ to $5 \text{ M}\Omega$ at 10 V as described earlier. Similar procedure was used for calibrating the load current separately for each channel. Subsequently, the fitted parameters obtained for each sub-range of voltage and current were stored into the micro-controller for each channel.

Once the calibration parameters for each channel were obtained; the system should be validated by sending the desired voltage (V_{set}) and then comparing it with the measured output voltage (V_{out}) across load and sense resistor by using Equation (1). Similarly, the load current estimated using the ADC counts should be compared with the *true* load current measured using Keithley pico-ammeter. This was accomplished in the validation run where the desired voltage in steps of 0.5 V was sent to the micro-controller. At each voltage (V_{set}), corresponding DAC count was calculated using the calibration parameters and sent to the DAC. The voltage appearing across the load, current flowing through the load and the ADC counts were recorded at each set voltage using the same procedure as described in the calibration run. In Fig. 4(c) the distribution of difference between the set and the measured output voltage (V_{out}) is shown. The width of this distribution from a Gaussian fit is observed to be 5 mV . This clearly demonstrated the programmable capability of the system to generate the desired voltage across the load with requisite precision. The load current was estimated using the recorded ADC counts at each voltage and the current calibration parameters obtained from the calibration run. In Fig. 4(d) the difference between *true* load current and the estimated load current from ADC counts is shown. The width of this distribution from a Gaussian fit was found to be 0.4 nA comparable to the design goal of 1 nA .

B. Load regulation and stability

Each channel of the PPS system was designed to provide required voltage with a resolution of 6.25 mV in the range $0\text{--}90 \text{ V}$, with a driving capacity of $32 \mu\text{A}$, significantly higher than the required current of 150 nA for a SiPM. The current capacity and effectiveness of voltage regulation was measured by the change in the output voltage at varying ohmic load for a given voltage. The load characteristic of one channel at different voltages is shown in Fig. 5. As seen from this figure,

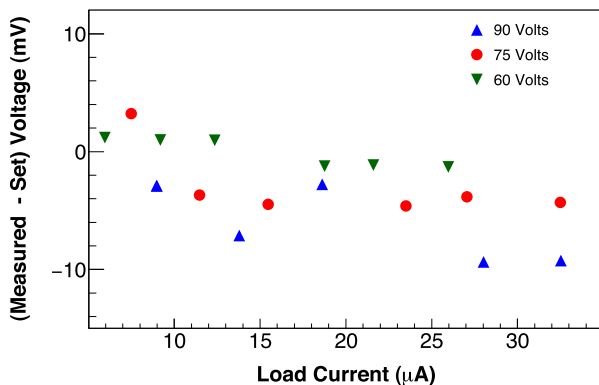


FIG. 5. Load regulation characteristics of one of the PPS channels.

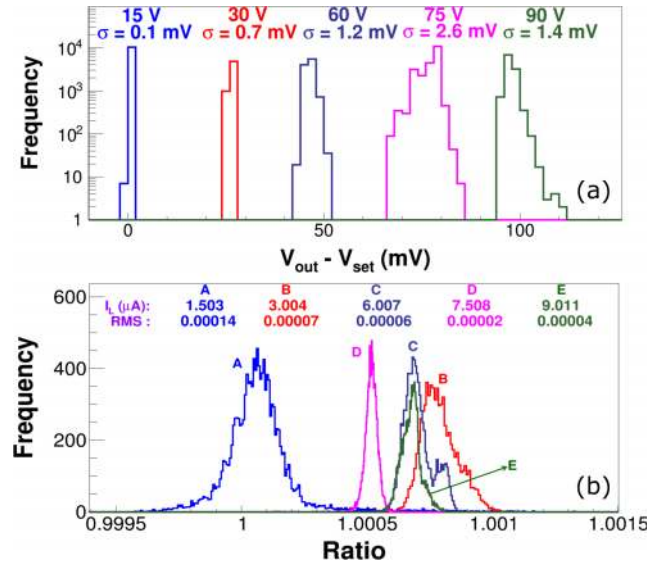


FIG. 6. Results of PPS stability at different applied voltages; (a) distribution of difference between applied and measured voltage. An offset of 25 mV was introduced between successive distribution for better visibility. (b) Distribution of ratio of PPS current to *true* current.

the difference between applied and *true* voltage was small up to the load current of $32 \mu\text{A}$ over the entire range of voltages, thus, validating the driving capability of the PPS.

With successful calibration and load regulation of the PPS system, it became important to investigate the long-term stability of this system. For this purpose, similar experimental setup as shown in Fig. 3 without external $10 \text{ M}\Omega$ load was used to carry out stability studies. It is to be noted that, the input impedance of K2000 voltmeter ($10 \text{ M}\Omega$ beyond 10 V) was the only effective load experienced by the PPS system. A fixed voltage was set at the channel under test and at this voltage, *true* voltage, *true* current, and the current measured using PPS system were logged continuously for 12 h . Data were recorded at different voltages in the range of $15\text{--}90 \text{ V}$. In Fig. 6(a) the distribution of difference between the applied and *true* voltage is shown at different applied voltages. As expected, the difference is consistent with zero with a rms deviation of 2.6 mV . In Fig. 6(b) the distribution of the ratio of current measured by PPS and *true* current for different set of applied voltages is shown. The mean value is consistent with unity with a rms deviation of 0.2 nA . This clearly establishes that the stability achieved in generating the voltage and current was well within the design parameters listed in Table I.

IV. SiPM RESPONSE WITH PPS SYSTEM

With the successful validation of the performance of the PPS system, it was used to measure the response of SiPM to pulsed laser light with and without thermal compensation of *over voltage*. In Fig. 7 the block diagram of the experimental setup is shown. The SiPM, pre-amplifier, temperature sensor, and the laser diode were enclosed in a light-tight metal box. The setup was operated at 20°C , referred as the base temperature. The SiPM was biased at 72.2 V ($\sim 1.5 \text{ V}$ above breakdown voltage), and excited by a pulsed laser diode (λ

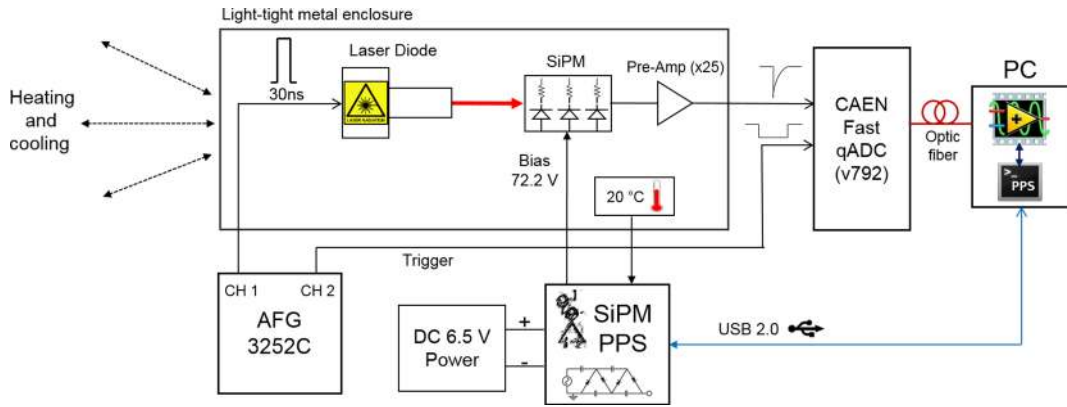


FIG. 7. Experimental setup used to record SiPM response to pulsed laser light.

~ 635 nm). Fast analog output pulses from SiPM were amplified by a pre-amplifier and then integrated and digitized with a VME based fast charge to digital converter (qADC v792 from CAEN). An arbitrary waveform generator was used to drive the laser diode as well as to trigger the input to the qADC synchronously at a rate of 1 KHz. The trigger pulse width was set at 120 ns for gated integration of SiPM pulses. The intensity of the laser was kept sufficiently low to clearly identify peaks due to single and higher number of *photo-electron* (*p.e.*). A dedicated LabVIEW¹⁹ framework and PPS control software was developed to operate this setup, to acquire data from the VME system and slow control data from PPS system.

A typical run of 20 000 triggers recorded integrated charge from SiPM. As shown in Fig. 8(a), multi-Gaussian fit to the integrated charge distribution was used to obtain the gain of the SiPM. First peak represents the inherent noise of the system and offsets in the qADC module. This peak is called the *pedestal peak*. The second peak represents events due to single pixel triggering, and referred as the *1 p.e. peak*. Third peak is due to two simultaneous pixel triggering and is termed as the *2 p.e. peak*. These peaks were used to obtain the gain of the SiPM using

$$\text{Gain} = 1/3 (1 \text{ p.e. peak} + 2 \text{ p.e. peak} - 2 \times \text{ped peak}). \quad (2)$$

A. Temperature dependence of SiPM gain

As discussed in Section I, the gain of SiPM strongly depends upon the ambient temperature. The dependence of the SiPM gain on temperature was obtained by recording its response without activating temperature compensation mechanism. The bias voltage on one channel of PPS connected to SiPM was set at 72.2 V and was not changed irrespective of the ambient temperature. The experimental setup for SiPM gain measurement is shown in Fig. 7. An external heating element was added to the metal enclosure to heat the setup up to 35 °C from a temperature of 20 °C. The system was allowed to cool without the aid of external cooling. During the entire heating and cooling cycle, slow control parameters such as ambient temperature, applied bias voltage, and current flowing in SiPM were recorded by the PPS control software every second. The response of the SiPM (digitized charge due to pulse from SiPM) to light pulses from laser diode was recorded by LabVIEW¹⁹ framework in each run of 20 K events every 30 s.

The recorded data were analyzed using ROOT framework.²⁰ The charge (qADC) distribution for each run was fitted using multi-Gaussian function to estimate *pedestal*, *1 p.e. peak*, *2 p.e. peaks* etc. Using these fitted values the gain of SiPM in each run was obtained by using Equation (2). Data from the heating cycle were not considered since the system takes a longer time to reach thermal equilibrium compared to the rate of heating. In Figs. 8(a) and 8(b), the SiPM charge distribution at 20 °C and 34.5 °C, respectively, without thermal compensation are shown. It is seen that the gain of SiPM (difference between successive peaks) reduces significantly at higher temperature. The SiPM gain was obtained from each run of 20 K events for

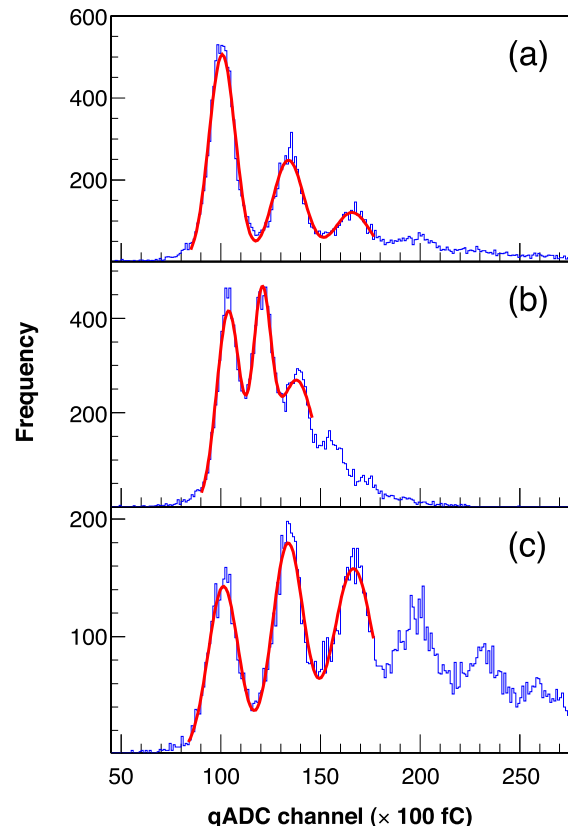


FIG. 8. Distribution of SiPM response to pulsed laser light at (a) 20 °C, (b) at 34.5 °C without temperature compensation, and (c) at 34.5 °C with temperature compensation. The distributions have been fitted with multi-peak Gaussian function.

a temperature range of 20–35 °C. Variation in gain as a function of temperature without thermal compensation is shown in Fig. 9(a). It is seen that the gain reduces by 50% when temperature increases from 20 to 35 °C.

B. Temperature compensation of SiPM gain

Such a large variation of the gain is unacceptable in most of the experiments that use SiPM as a photon detector. To stabilize the SiPM gain, an algorithm for thermal compensation programmed in the micro-controller was activated. A temperature coefficient of 56 mV/°C for breakdown voltage was stored in the micro-controller. In the beginning, SiPM bias was set to 72.2 V at 20 °C which was treated as the base temperature (T_b). Bias voltage (equivalent DAC counts) was evaluated dynamically with temperature feedback loop using

$$V_{bias} = 72.2 + 0.056(T - T_b). \quad (3)$$

When the measured temperature changed by more than 0.1 °C, a revised DAC count was estimated and loaded into the DAC to generate a corresponding bias voltage to maintain a

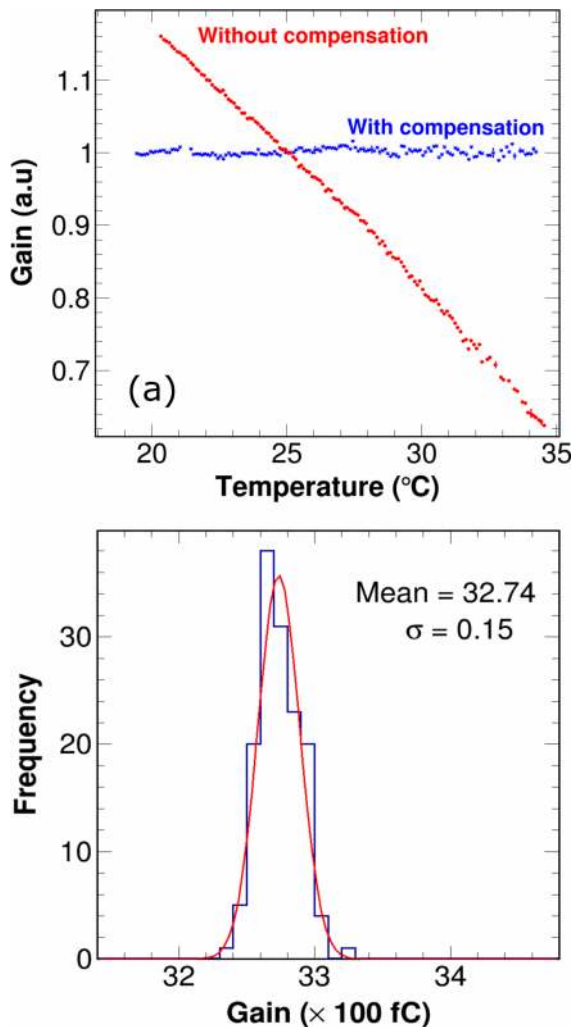


FIG. 9. (a) Variation of gain, with (blue) and without (red) compensation algorithm. Gain was normalized to the value at 25 °C. (b) Distribution of SiPM gain over a temperature range of 15 °C with temperature compensation enabled. A gain stability of 0.5% was achieved.

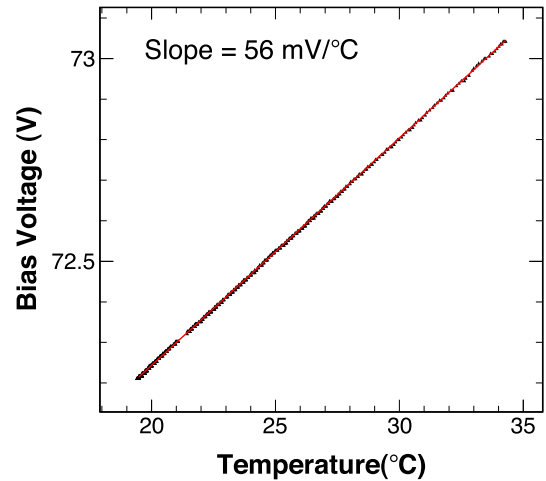


FIG. 10. Variation of bias voltage generated by SiPM PPS as a function of temperature. The set temperature coefficient was reproduced in the data.

constant *over voltage*. Slow control parameters and SiPM data were taken and analyzed with a similar thermal cycle as was described in Section IV A. It is to be noted that the applied voltage changes with temperature as shown in Fig. 10. The slope obtained from this plot is in excellent agreement with the set thermal coefficient of 56 mV/°C demonstrating that thermal compensation scheme functioned exactly as designed. In Figs. 8(a) and 8(c) the SiPM charge distribution at 20 and 34.5 °C, respectively are shown. It is seen that there was no significant change in the SiPM gain, thus, establishing the desired functionality of the thermal compensation mechanism of the PPS system. Also, at higher temperatures, the amplitude of 2nd, 3rd... peaks were found to be higher when compared to that at room temperature (20 °C), which was due to cumulative effect of changes in dark count rate,¹ cross talk, after pulsing and photon detection efficiency including possibility of non-stability of laser diode at higher temperature. In Fig. 9(a), gain of the SiPM normalized to its gain at 25 °C, measured at different temperatures with and without temperature compensation scheme are shown. The gain was found to be constant over a temperature range of 15 °C with thermal compensation. The distribution of SiPM gain, recorded in the range of 20–35 °C with thermal compensation is shown in Fig. 9(b). The gain stability, defined as the ratio of $\sigma/mean$, was observed to be 0.5% over a range of 15 °C. Hence, an excellent stability of the SiPM gain over a wide range of temperature was demonstrated by the PPS system.

V. CONCLUSIONS

The SiPM has a number of advantages compared to vacuum PMTs and thus, is being considered a superior replacement over bulky PMTs. However, the breakdown voltage of the SiPM critically depends on the ambient temperature thereby significantly affecting the gain (3%–5%/°C) of the device. The gain of this device can be stabilized over a wide range of temperatures by maintaining a constant *over voltage*. A programmable high resolution temperature compensating power supply for application in the GRAPES-3 experiment

was designed and many of the rigorous tests were carried out to benchmark the performance of this system. The PPS system was subjected to extensive calibration against standard voltage and current meters from Keithley. The voltage and current precision of this system were established to be well within the design specifications. The load regulation and stability tests were carried out to ensure uninterrupted use of the PPS system over a prolonged period with adequate driving capacity. Studies carried out on the gain of a SiPM has shown a stability of 0.5% over a wide temperature range (15 °C) could be achieved. Thus, the PPS system can be used in the GRAPES-3 experiment to readout scintillation light from a large array of scintillators operating in an outdoor environment. The flexible and scalable system design offers an easy to operate user interface and expansion possibility via Daisy chaining on the I^2C bus. Multi-channel PPS system being compact and light-weight can also be used in Imaging Cerenkov Telescopes with SiPM being used as photo-readout element.²¹ If required, a non-linear thermal response of other devices can also be encoded into the PPS system, thus, widening the scope of this system well beyond GRAPES-3 experiment.

ACKNOWLEDGMENTS

We thank V. M. Aaranke for his help and useful discussions during this project. We thank Mr. S. Chavan for his help in making mechanical fixtures for the setup used here and Mr. S. R. Chendvankar for providing high precision voltmeter used in calibration and stability verification tests of PPS system. We thank all members of the GRAPES-3 collaboration for their interaction.

¹N. Dinu, C. Bazin, C. Chaumat, C. Cheikali, A. Para, V. Puill, C. Sylvia, and J.-F. Vagnucci, in *IEEE Nuclear Science Symposium, Medical Imaging Conference and 17th Room Temperature Semiconductor Detector Workshop* (IEEE, 2010), p. 215.

²S. Gupta, Y. Aikawa, N. Gopalakrishnan, Y. Hayashi, N. Ikeda, N. Ito, A. Jain, A. John, S. Karthikeyan, S. Kawakami, T. Matsuyama, D. Mohanty, P. Mohanty, S. Morris, T. Nonaka, A. Oshima, B. Rao, K. Ravindran, M. Sasano, K. Sivaprasad, B. Sreekantan, H. Tanaka, S. Tonwar, K. Viswanathan, and T. Yoshikoshi, *Nucl. Instrum. Methods Phys. Res., Sect. A* **540**, 311 (2005).

³P. Finocchiaro, A. Pappalardo, L. Cosentino, M. Belluso, S. Billotta, G. Bonanno, and S. Di Mauro, *IEEE Trans. Nucl. Sci.* **56**, 1033 (2009).

⁴D. Renker and E. Lorenz, *J. Instrum.* **4**, P04004 (2009).

⁵S. I. Kwon, J. S. Lee, H. S. Yoon, M. Ito, G. B. Ko, J. Y. Choi, S.-H. Lee, I. Chan Song, J. M. Jeong, D. S. Lee, and S. J. Hong, *J. Nucl. Med.* **52**, 572 (2011).

⁶S. J. Hong, H. G. Kang, G. B. Ko, I. C. Song, J.-T. Rhee, and J. S. Lee, *Phys. Med. Biol.* **57**, 3869 (2012).

⁷Y. Lu, K. Yang, K. Zhou, Q. Zhang, B. Pang, and Q. Ren, *Nucl. Instrum. Methods Phys. Res., Sect. A* **743**, 30 (2014).

⁸P. Buzhan, B. Dolgoshein, L. Filatov, A. Ilyin, V. Kantzerov, V. Kaplina, A. Karakash, F. Kayumov, S. Klemm, E. Popova, and S. Smirnov, *Nucl. Instrum. Methods Phys. Res., Sect. A* **504**, 48 (2003).

⁹J. Anderson, J. Freeman, S. Los, and J. Whitmore, in *Proceedings of the 2nd International Conference on Technology and Instrumentation in Particle Physics (TIPP 2011)* [*Phys. Procedia* **37**, 72 (2012)].

¹⁰J. Freeman, *Nucl. Instrum. Methods Phys. Res., Sect. A* **617**, 393 (2010).

¹¹H. Miyamoto, M. Teshima, B. Dolgoshein, R. Mirzoyan, J. Nincovic, and H. Krawczynski, in *Proceedings of ICRC (LODZ, Poland, 2009)*, Vol. 31, p. 1320.

¹²M. Yokoyama, T. Nakaya, S. Gomi, A. Minamino, N. Nagai, K. Nitta, D. Orme, M. Otani, T. Murakami, T. Nakadaira, M. Tanaka, Y. Kudenko, F. Retiere, and A. Vacheret, in *New Developments in Photodetection [NDIP08Proceedings] of the Fifth International Conference on New Developments in Photodetection* [*Nucl. Instrum. Methods Phys. Res., Sect. A* **610**, 128 (2009)].

¹³Y. Hayashi, Y. Aikawa, N. Gopalakrishnan, S. Gupta, N. Ikeda, N. Ito, A. Jain, A. John, S. Karthikeyan, S. Kawakami, H. Kojima, T. Matsuyama, D. Mohanty, P. Mohanty, S. Morris, T. Nonaka, A. Oshima, B. Rao, K. Ravindran, M. Sasano, K. Sivaprasad, B. Sreekantan, H. Tanaka, S. Tonwar, K. Viswanathan, and T. Yoshikoshi, *Nucl. Instrum. Methods Phys. Res., Sect. A* **545**, 643 (2005).

¹⁴R. Shukla, S. Dugad, C. Garde, A. Gopal, S. Gupta, and S. Prabhu, *Rev. Sci. Instrum.* **85**, 023301 (2014).

¹⁵MPPC Technical Information, Online: https://www.hamamatsu.com/resources/pdf/ssd/mppc_kapd9003e.pdf.

¹⁶Z. Li, Y. Xu, C. Liu, Y. Li, M. Li, Y. Chen, Y. Wang, B. Lu, W. Cui, J. Huo, T. Chen, D. Han, W. Hu, C. Li, W. Li, X. Liu, J. Wang, Y. Yang, Y. Zhang, Y. Zhu, G. Li, J. Zhao, J. Wang, N. Pu, and X. Li, in *New Developments in Photodetection [NDIP11]* [*Nucl. Instrum. Methods Phys. Res., Sect. A* **695**, 222 (2012)].

¹⁷F. Licciulli, I. Indiveri, and C. Marzocca, *IEEE Trans. Nucl. Sci.* **60**, 606 (2013).

¹⁸P. Dorosz, M. Baszczyk, S. Glab, W. Kuczewicz, L. Mik, and M. Sapor, in *Proceedings of the 12th Pisa Meeting on Advanced Detectors La Biodola, Isola Elba, Italy, 20–26 May 2012* [*Nucl. Instrum. Methods Phys. Res., Sect. A* **718**, 202 (2013)].

¹⁹LabVIEW System Design Software, Online: <http://www.ni.com/labview/>.

²⁰ROOT, Object-Oriented Data AnalySiS Framework. Online: <http://root.cern.ch>.

²¹A. Biland, T. Bretz, J. Bu, V. Commichau, L. Djambazov, D. Dorner, S. Einecke, D. Eisenacher, J. Freiwald, O. Grimm, H. von Gunten, C. Haller, C. Hempfling, D. Hildebrand, G. Hughes, U. Horisberger, M. L. Knoetig, T. Krähenbühl, W. Lustermaan, E. Lyard, K. Mannheim, K. Meier, S. Mueller, D. Neise, A. K. Overkemping, A. Paravac, F. Pauss, W. Rhode, U. Röser, J. P. Stucki, T. Steinbring, F. Temme, J. Thaele, P. Vogler, R. Walter, and Q. Weitzel, *J. Instrum.* **9**, P10012 (2014).